

Photoelectrochemical Study on Charge Transfer Properties of TiO₂–B Nanowires with an Application as Humidity Sensors

Geng Wang, Qiang Wang, Wu Lu, and Jinghong Li*

Department of Chemistry, Key Laboratory of Bioorganic Phosphorus Chemistry and Chemical Biology, Tsinghua University, Beijing 100084, China

Received: July 21, 2006; In Final Form: August 29, 2006

One-dimensional (1-D) TiO₂–B nanowires have been synthesized via a facile solvothermal route. The morphology and crystalline structures of the nanowires were characterized by using powder X-ray diffraction, low/high-resolution transmission electron microscopy, and Brunauer–Emmett–Teller methods. It is important with the calcination treatment at 350 °C to maintain 1-D morphologies of the material in the form of single-crystalline TiO₂–B nanowires. In addition, a simple method was used to study the photogenerated charge transfer and photoelectrochemical properties of the TiO₂–B nanowires in comparison with commercial TiO₂ P25 nanoparticles based on the experimental data from the electric field-effected photocurrent action spectrum and Mott–Schottky measurements. It was revealed that TiO₂–B nanostructures played an important role in the photoelectrochemical processes. The synthetic TiO₂–B nanowire electrode exhibited unique electronic properties, e.g., favorable charge-transfer ability, negative-shifted appearing flat-band potential, existence of abundant surface states or oxygen vacancies, and high-level dopant density. Moreover, the obtained TiO₂–B nanowires were found to display excellent humidity sensing abilities as functional materials in the humidity sensor application. With relative humidity increased from 5% to 95%, about one and half orders of magnitude change in resistance was observed in the TiO₂–B nanowire-based surface-type humidity sensors.

1. Introduction

Recently, 1-D nanostructured TiO₂ such as nanorods, nanobelts, nanowires, and nanotubes have attracted intensive research interests due to their size and morphology dependent physicochemical properties and potential applications, e.g., optoelectronic devices,¹ chemical sensors,² photochromic devices,³ batteries,⁴ and supercapacitors,⁵ besides which the photoinduced activities of TiO₂ nanostructures play an important role in the applied fields such as photovoltaics, photocatalysis, and photoinduced superhydrophilicity.⁶ It has been known that TiO₂ nanotubes and nanowires may be synthesized through the reactions between different TiO₂ precursors and concentrated NaOH solution under moderate hydrothermal conditions in relatively large quantities.⁷ Armstrong et al. reported that the as-synthesized TiO₂ nanotubes and nanowires were sodium hydrogen titanates of general formula Na_yH_{2–y}Ti_nO_{2n+1}·xH₂O. Acid washing of such materials resulted in ion exchange to produce the layered hydrogen titanates H₂Ti_nO_{2n+1}·xH₂O, which may be converted to the titanium dioxide polymorph TiO₂–B on heating.⁸ TiO₂–B is the least dense polymorph of TiO₂ with a shear derivative of the ReO₃ type structure.⁹ It has the advantage over the other titanium dioxide polymorphs of being a relatively open structure with significant voids and continuous channels, making the TiO₂–B structure an excellent host for Li intercalation, and leading to nanowires that can display simultaneously n-type electronic conductivity and lithium-ion transport.⁸ TiO₂–B based nanotubes and nanowires showed attractive performance in rechargeable lithium batteries.^{10–12} Also high photocatalytic activity was observed by using TiO₂ nanostructure with polycrystalline phase containing anatase and

TiO₂–B.¹³ Hence TiO₂–B structures should play an important role in various applications. However, until recently it was still rare to study the photoelectrochemical (PEC) properties of TiO₂–B nanostructures.

During past decades the research interests on the phenomena of electron transfer across a semiconductor–liquid interface show dramatic growth due to increasing requirements of solar energy conversing applications.¹⁴ In particular, recent study on nanostructure-based highly oriented nanoarrays is crucial for the development of novel applications due to the enhancement of the electron-transfer properties by providing direct conduction paths for the electrons from the point of injection to the collection electrode while still maintaining high surface-to-volume ratio.¹⁵ But still the fundamental factors that control the electron transfer across the semiconductor–electrolyte interfaces in a PEC cell are poorly elucidated. Moreover, the relatively simple and low-cost experimental techniques for detecting the recombination of the photogenerated charge carriers and charge-transfer properties at the surface of the solid, and at the solid–liquid contact, are still not well-developed.

In this work, TiO₂–B nanowires were synthesized through a facile solvothermal method followed with acid-washing and annealing treatments. By investigating the PEC properties of the synthetic TiO₂–B nanowires in comparison with commercial TiO₂ P25 nanoparticles, we studied the photogenerated charge transfer and electric properties of TiO₂ nanostructured electrodes using experimental techniques such as photocurrent action spectrum (PAS) and electric field-effected photocurrent action spectrum (EFEPAS) together with Mott–Schottky (MS) techniques. Furthermore, a TiO₂ nanostructure-based surface-type humidity sensor was fabricated, and its unprecedented humidity sensing abilities revealed the excellent characteristics of the TiO₂–B nanowires, consistent with the above proposed proper-

* Address correspondence to this author. E-mail: jhli@mails.tsinghua.edu.cn. Phone and fax: +86-10-62795290.

ties based on PEC measurements. The study assists in addressing the relationship between the nanostructures and their PEC characteristics, and it is significant for understanding the unique properties that result from their size and morphology and designing novel nanostructures with advanced applications.

2. Experimental Section

2.1. Solvothermal Synthesis. TiO_2 nanowires were synthesized by dispersing 2 g of TiO_2 (Degussa P25, which consists of about 30% rutile and 70% anatase and a particle size of about 20 nm) in 60 mL of mixed solvents of 10 M NaOH aqueous solution and ethanol, with the volume ratio of NaOH aqueous solution to ethanol being 1:1. After the solution was stirred for 1 h, the resulting suspension was transferred into a Teflon-lined stainless steel autoclave. The autoclave was maintained at 180 °C for 18 h and then cooled to room temperature naturally. The resulting white precipitate was recovered by centrifugation and washed with 0.1 M HCl solution and deionized water several times until pH 7, and kept for further characterization.

2.2. Material Characterization. Before all characterizations, the synthetic materials were calcinated at 350 °C for 4 h in air. Power X-ray diffraction (XRD) was performed on a Bruker D8-Advance X-ray powder diffractometer with monochromatized Cu $\text{K}\alpha$ radiation ($\lambda = 1.5418 \text{ \AA}$). The 2θ range used in the measurements was from 10° to 70°. Transmission electron microscopy (TEM) images were taken with a Hitachi model H-800 transmission electron microscope, using an accelerating voltage of 200 kV. The structure and composition of the nanowires were measured by high-resolution transmission electron microscopy (HRTEM, JEOL-2010F). Specific surface areas were measured by Brunauer–Emmett–Teller (BET) nitrogen adsorption–desorption (Shimadzu, Micromeritics ASAP 2010 Instrument), and pore size distributions were calculated from the desorption branch of the N_2 adsorption isotherm, using the Barrett–Joyner–Halenda (BJH) formula.

2.3. Photoelectrochemical Measurements. TiO_2 nanomaterial paste for the fabrication of photoanode was obtained by mixing 2 mL of ethanol and 300 mg of TiO_2 nanomaterial powder homogeneously. The TiO_2 suspension was spread on the FTO conducting glass (15 Ω/square F-doping SnO_2) with a glass rod, using adhesive tapes as spacers. After the films were dried under ambient conditions, they were sintered in air at 350 °C for 4 h. The film thickness measured with a profilometer was ca. 3 μm . PAS were measured in a two-electrode configuration home-built experimental system, where the sintered TiO_2 photoanode served as the working electrode with the active area of ca. 1 cm^2 by using Teflon tape and a platinum wire was used as the counter electrode. A 500-W Xe lamp with a monochromator was used as the light source. The PEC cell was illuminated from the FTO side of the TiO_2 electrode by incident light. The generated photocurrent signal was collected by using a lock-in amplifier (Stanford instrument SR830 DSP) synchronized with a light chopper (Stanford instrument SR540). The monochromatic illuminating light intensity was about 15 $\mu\text{W}/\text{cm}^2$ estimated with a radiometer (Photo-electronic Instrument Co. IPAS). The illumination area of the TiO_2 electrode was about 0.12 cm^2 . All measurements were done after bubbling N_2 for 20 min and controlled automatically by computer.

EFEPAS is a combined technique based on the field effect principle and PAS technique.⁹ With a DC electric field applied to both electrodes of a PEC cell, the mobile direction and diffusive distance of photogenerated charge carriers can be modified, and the build-in field on the sample surface also changes. The electric field affects the photoresponse of the

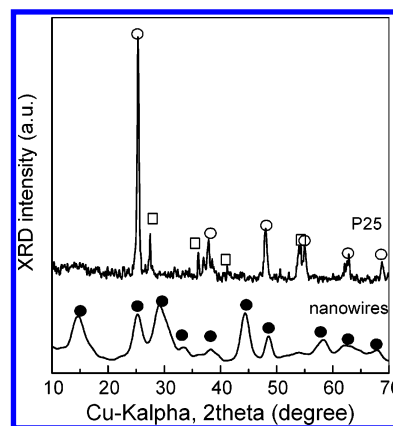


Figure 1. X-ray diffraction patterns of TiO_2 -B nanowires and TiO_2 P25 nanoparticles prepared by annealing at 350 °C for 4 h in air (solid circles: TiO_2 -B; open circles: anatase; and open squares: rutile).

sample in two ways: (i) in the dark state, the field-effected motion of the free and semilocalized charge carriers influences the charge carrier density in the space-charge region and (ii) in the illuminating state, the polarity and intensity of the external applied electric field control the mobile direction of the photogenerated charge carriers and their diffusion length. Both factors directly affect the intensity of the photovoltaic characteristics. Thus, using the EFEPAS technique, the photoinduced charge transfer process can be clearly detected.

2.4. Mott–Schottky Measurements. Mott–Schottky spectra were measured with a three-electrode cell, using the sintered TiO_2 photoanode as the working electrode, a platinum wire as the counter electrode, and a standard Ag/AgCl in saturated KCl as the reference electrode. The electrolyte was 0.05 M KCl (pH 7.5). Impedance spectra were obtained with a PARSTAT-2273 Advanced Electrochemical System (Princeton Applied Research) equipped with an impedance analyzer with ZSimpWin software and controlled by a computer.

2.5. Humidity Sensors Fabrication and Tests. Surface-type humidity sensors were fabricated by the same technique for the photoanode preparation by using TiO_2 nanostructure paste on the FTO substrates with interdigital electrodes (gap distance 50 μm) prepared with photolithographic technique. Before measurements, the samples were sintered at 350 °C for 4 h. Humidity sensitive characterization was done with a home-designed system; the relative humidity (RH) could be changed in the range of 5–95%, using the mixture of dry and wet nitrogen.¹⁶ The RH values were calibrated by using a commercial humidity sensor (Testo AG 635-1). Electrical signals were measured by the PARSTAT-2273 Advanced Electrochemical System.

3. Results and Discussion

TiO_2 nanowires were synthesized by using a facile solvothermal method as described in the Experimental Section. After being washed with dilute acid and heated, the as-synthesized titanate nanowires converted to TiO_2 -B but retained their cylindrical morphology. Figure 1 shows the powder X-ray diffraction (XRD) patterns of the TiO_2 P25 nanoparticles and acid-washed TiO_2 nanowires after calcination at 350 °C for 4 h in air. Consistent with the product report, all diffraction peaks of TiO_2 P25 could be characterized as anatase and rutile, respectively. And anatase was the major phase, which was in agreement with the informed amount (70%). The relatively broad diffraction peaks of TiO_2 nanowires were due to dimensional confinement as compared to that of bulk counter-

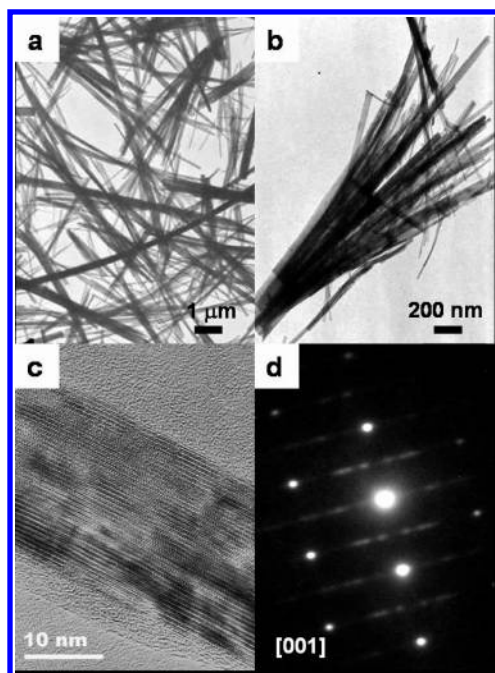


Figure 2. Variable magnification TEM images of the TiO₂-B nanowires (a and b), HRTEM lattice image (c), and ED pattern of the TiO₂-B nanowires (d).

parts.¹⁰ All diffraction peaks of TiO₂ nanowires after sintering at 350 °C could be indexed as TiO₂-B characterized by corrugated sheets of corner- and edge-sharing TiO₆ octahedra linked together by bridging oxygen atoms.⁸ Thus, indeed through this simple solvothermal route, we are able to obtain single-crystalline TiO₂-B nanowires.

Evidence that the TiO₂-B nanowires have retained their morphology is shown in Figure 2. The transmission electron microscopy (TEM) images of the synthetic nanowires in different magnification are shown in Figure 2a,b. TiO₂-B nanowires were observed with diameters of about 20–50 nm and lengths of up to several micrometers (Figure 2a). Some broomlike morphology has been observed too. Figure 2b shows a bundle of nanowires splitting on the same root, which is a piece of crystalline sheet. High-resolution TEM (HRTEM) and the corresponding selected area electron diffraction (ED) pattern investigations provide further insight into the fine microstructure and crystallinity (Figure 2c,d). A typical HRTEM image recorded on a single nanowire (Figure 2c) shows a well-crystallized structure with lattice fringes of about 0.65 nm, corresponding to an interplanar spacing of TiO₂-B. The corresponding ED pattern (Figure 2d) could be completely indexed in the monoclinic *C2/m* space group, using the bulk TiO₂-B unit cell parameters with $a = 1.21787$ nm, $b = 0.37412$ nm, $c = 0.65249$ nm, and $\beta = 107.054^\circ$.¹⁷ The superlattice reflections confirm that the nanowires grow preferably along the [001] direction.

The nitrogen adsorption/desorption isotherms at 77 K and pore size distributions of TiO₂-B nanowires and P25 nanoparticles are presented in Figure 3. Considering the absence of nitrogen adsorption at very low pressure, it can be concluded that the micropore contribution to the total pore volume was negligible for the two materials. As seen from Figure 3a, the adsorption curve gradually increased in the middle-pressure region and exhibited abruptly in the high-pressure region ($>0.8P/P_0$), so the adsorption behavior of TiO₂ P25 can be attributed to the capillary condensation and multilayer adsorption of nitrogen in the mesopores or macropores.¹⁸ As for TiO₂-B

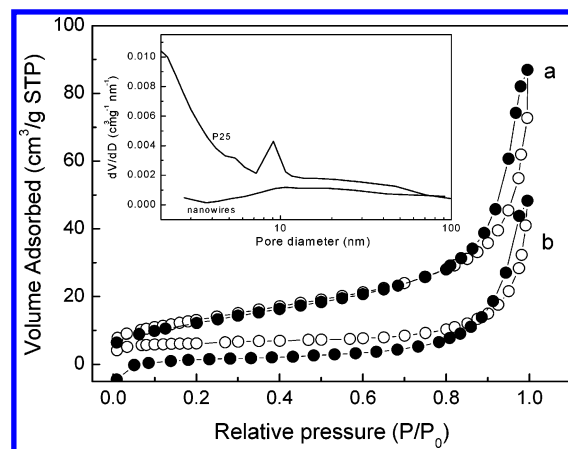


Figure 3. The N₂ adsorption and desorption isotherms of P25 nanoparticles (a) and TiO₂-B nanowires (b). Solid circles: adsorption; hollow circles: desorption. The inset shows BJH pore-size distributions of two nanostructures.

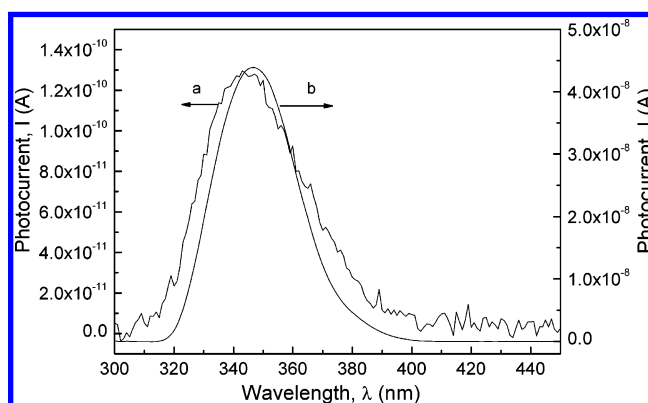


Figure 4. Photocurrent spectra of (a) TiO₂-B nanowire and (b) TiO₂ P25 nanoparticle electrodes.

nanowires, reasonably they exhibited the adsorption characteristics of nonporous or macroporous materials. These conclusions can be good agreement with Barrett–Joyner–Halenda (BJH) pore size distributions of TiO₂-B nanowires. The values of Brunauer–Emmett–Teller (BET) surface area can be determined as 47.6 m²/g for P25 and 17.8 m²/g for the nanowires.

Since TiO₂ is the most commonly used electrode material in PEC cells and optoelectronics, for understanding the PEC properties of the synthesized TiO₂-B nanowires, PAS measurements were performed. For comparison, the TiO₂ P25-based photoanode was also studied. The results are shown in Figure 4. As shown from curve b, the TiO₂ P25 electrode showed a photocurrent spectrum with the maximum wavelength at 347 nm corresponding to the band-gap of nanocrystalline TiO₂, which is blue-shifted from the band-gap of bulk TiO₂ (387 nm, 3.2 eV) due to the quantum confinement effect. The PAS of the synthetic TiO₂-B nanowire electrodes kept a similar behavior as the nanoparticle layer with about 2 orders of magnitude lower photocurrent intensities. Furthermore, because of the quantum confinement effect, the photocurrent spectrum of TiO₂-B nanowires was slightly blue-shifted and the maximum wavelength remained at around 340 nm.

The transport of photogenerated electron through the n-type semiconductor nanostructured layer to the collecting electrode is believed to occur by diffusion within extended states slowed by trapping/detrapping events.¹⁹ It is known that the application of a potential to an ideally behaving semiconductor electrode interface effects a change in the observed current density by changing the value of the electron concentration at the surface

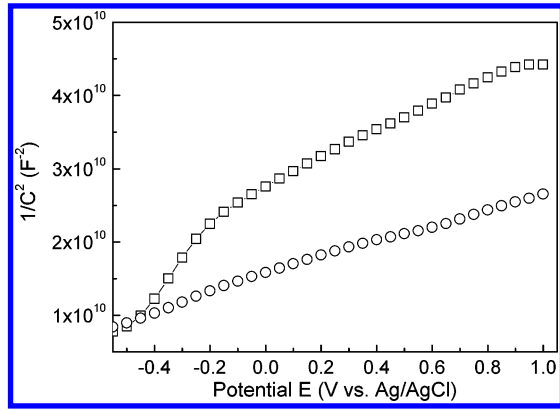


Figure 5. Mott-Schottky plots of TiO₂ P25 nanoparticle film (open squares) and synthetic TiO₂-B nanowire (open circles) electrodes. Mott-Schottky measurements were done at the frequency of 1 kHz in the aqueous solution of 0.05 M KCl, pH 7.5.

of the solid. To further characterize the electron-transfer properties of the synthesized TiO₂ nanostructure-based electrodes, MS and EFEPAS measurements were performed.²⁰ Figure 5 shows the MS spectra of the TiO₂ P25 nanoparticle and synthetic TiO₂-B nanowire electrodes. A reversed sigmoidal plot was observed with an overall shape consistent with that typical for n-type semiconductors.²¹

As we know from the classical Mott-Schottky theory,²⁰ when the doping semiconductor space-charge region is in depletion as it is under biasing conditions, the capacitance of the space-charge region can be described after simplification as

$$\frac{1}{C^2} = \left(\frac{2}{eN_d\epsilon_0\epsilon} \right) |V - V_{fb}| \quad (1)$$

where e is the electronic charge unit, ϵ_0 is the permittivity of free space, ϵ is the dielectric constant, N_d is the dopant density (cm⁻³), V is the applied potential (V), and V_{fb} is the flat-band potential (V), i.e., the potential corresponding to the situation in which there is no charge accumulation in the semiconductor so that the energy bands show no bending. It shows that when $1/C^2$ is zero, the x -intercept is equal to the flat band potential V_{fb} , and the dopant density N_d can be determined from the slope of the linear region:

$$N_d = - \left(\frac{2}{e\epsilon_0\epsilon} \right) \left(\frac{d(1/C^2)}{dV} \right)^{-1} \quad (2)$$

However, in case of PEC cells where the FTO/semiconductor nanostructure-based film acts as a photoanode, because of the contact between the FTO substrate and the electrolyte permeating through the TiO₂ network voids, the situation is a bit different. Bisquert and Zaban et al. reported that the apparent flat-band potential, $V_{fb0} = -(V_{fb} + V_1)$, was shifted negatively from the real flat-band potential V_{fb} by an amount V_1 in the Mott-Schottky analysis of nanoporous TiO₂ electrodes, where $V_1 = N_d e \epsilon_0 \epsilon / 2 C_H^2$ and C_H is the Helmholtz capacitance of the electrode.²² Thus, in the nanoporous semiconductor photoelectrode case, the capacitance can be described as:

$$\frac{1}{C^2} = \left(\frac{2}{eN_d\epsilon_0\epsilon} \right) |V - V_{fb}| + \frac{1}{C_H^2} \quad (3)$$

Fortunately, the slope of C^{-2} vs V does not change with respect to that predicted in band-edge pinning conditions, $2/(N_d e \epsilon_0 \epsilon)$. Thus, we can still calculate the dopant density N_d using eq 2.

According to the data shown in Figure 5, the reproducible apparent flat-band potential V_{fb0} could be obtained from the x -intercept of the linear region of the curve C^{-2} vs V . The observed V_{fb0} for TiO₂ P25 and synthetic TiO₂-B nanowires samples are -0.60 and -1.11 V, respectively. Comparing with the P25 nanoparticle sample, the TiO₂-B nanowire shows a significantly negative shift in the apparent flat-band potential. Because of the same electrode fabricating and experimental processes, the deviation value V_1 is supposed to remain the same for both materials, thus, the real flat-band potential of TiO₂-B nanowires is also negatively shifted. The origin of this effect can be multifold. In most cases, it is provided that a large number of surface states or oxygen vacancies are available in the nanowires sample, leading to a change of the band position.²³ In our case, it seems the high level surfaces states (or oxygen vacancies), which are acting as charge carriers recombination centers or trapping states in the synthetic TiO₂-B nanowires, lead to the much lower photocurrent signals compared to the P25 sample. Moreover, comparing the slopes of the linear regions in MS spectra, the nanowires sample showed a much lower value, clearly indicating a much higher value of the dopant density in the nanowire electrode. According to eq 2, with the knowledge of $e = 1.6 \times 10^{19}$ C, $\epsilon_0 = 8.86 \times 10^{-12}$ F/m, and $\epsilon = 48$ F/m for TiO₂ materials,²⁴ the dopant density N_d of TiO₂ P25 and synthetic TiO₂-B nanowires can be calculated by using extracted slope of the linear regions from the data shown in Figure 5 as 5×10^{17} and 2×10^{18} cm⁻³, respectively.

EFEPAS of the TiO₂ P25 nanoparticle and TiO₂-B nanowire electrodes are shown in Figure 6. In a classical semiconductor-based PEC system, following the principles of charge transfer processes at a semiconductor photoelectrode, the net flux of electrons from the conductance band to randomly distributed acceptors in solution is given by the rate law:²⁵

$$J(V) = -ek_{et}[A]n_s \quad (4)$$

where J is the photocurrent density (A cm⁻²), k_{et} is the electron-transfer rate constant (cm⁴ s⁻¹), $[A]$ is the acceptor concentration (cm⁻³), and n_s is the electron concentration on the surface of the semiconductor (cm⁻³), which is related through a Boltzmann-type relationship to the difference between the potential applied to the electrode V and flat-band potential V_{fb} :

$$n_s = N_d \exp \left[\frac{e(V_{fb} - V)}{kT} \right] \quad (5)$$

where k is Boltzmann constant and T is the absolute temperature (K). By inputting eq 5 into eq 4, one can obtain

$$J(V) = -B \exp \left[\frac{e(V_{fb} - V)}{kT} \right] \quad (6)$$

where $B = ek_{et}[A]N_d$ (C cm⁻² s⁻¹) as an introduced parameter. If J is shown to follow eq 6, defined as the charge-transfer product $f = k_{et}[A]$ (cm s⁻¹), then f can be calculated with the knowledge of N_d and V_{fb} according to the following equation:

$$f = B/(eN_d) \quad (7)$$

As shown in Figure 6a, it was observed that in the case of the TiO₂ P25 nanoparticle electrode, as the external applied potential was increased from 0 to 1.5 V (photoanode, positive; Pt wire, negative), the maximum photocurrent density was decreased, and the data could be fitted well with a single-exponential function (correlation coefficient $R = 0.95$, see Figure

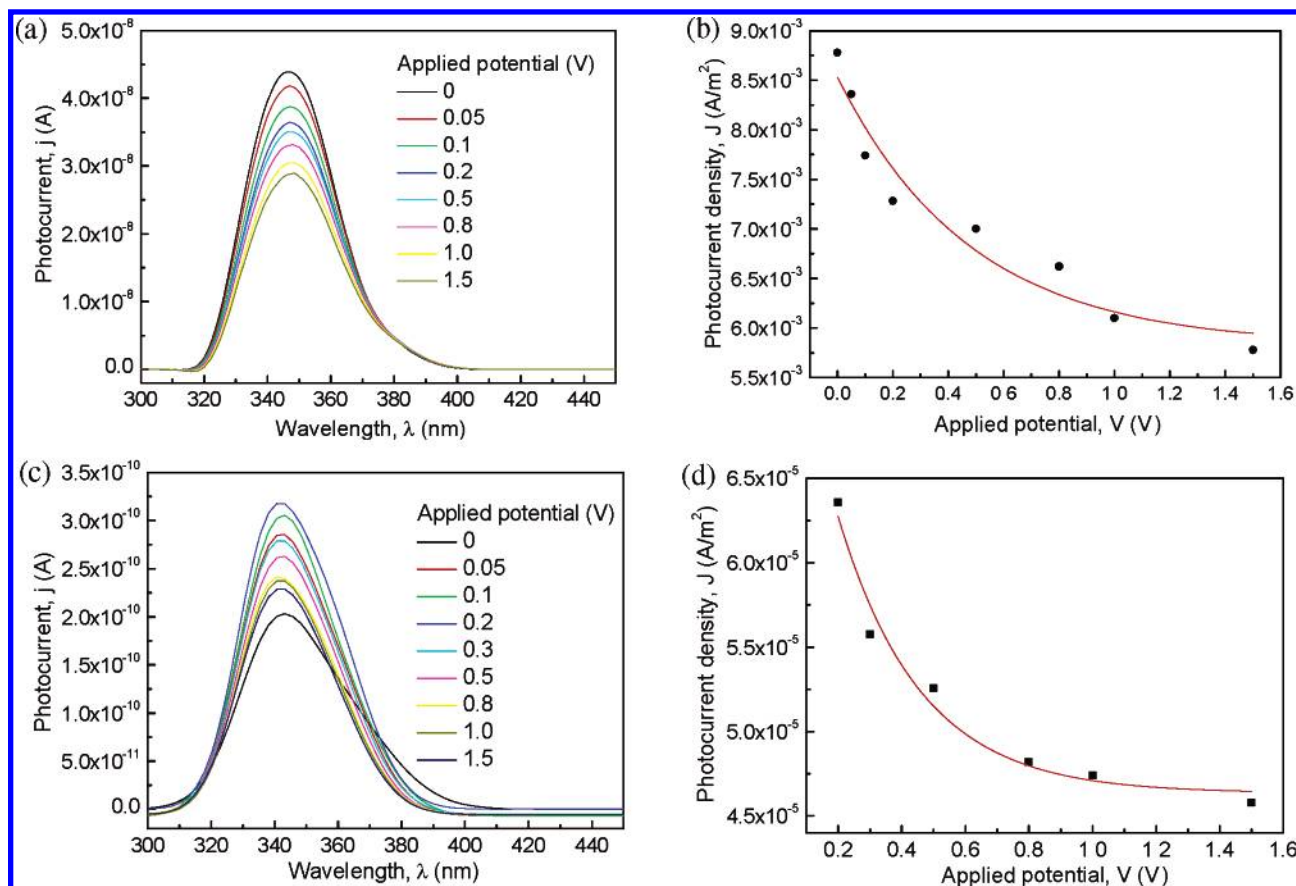


Figure 6. Electric field-effected photocurrent action spectra of (a) TiO₂ P25 nanoparticle and (c) TiO₂-B nanowire electrodes. Maximum photocurrent density vs external applied potential fitted by a single-exponential function of (b) P25 nanoparticle and (d) TiO₂-B nanowire electrodes.

6b). Following the fitted result $J = (-2.7 \times 10^{-3})\exp(-V/0.48)$, the constant B can be obtained as 2.7×10^{-3} (C cm⁻² s⁻¹). With the knowledge of $N_d = 5 \times 10^{17}$ cm⁻³ based on the above MS measurement results, the electron-transfer product f for the TiO₂ P25 nanoparticle electrode can be calculated with eq 7 as 3×10^7 (cm s⁻¹). Similar treatment can be used for calculating f of the synthetic TiO₂-B nanowire electrode as 1.3×10^{12} (cm s⁻¹) according to the data shown in Figure 6c,d. Assuming the acceptor concentration $[A]$ in the electrolyte is kept as a constant while the experimental system is fixed, it is clear to see that the charge-transfer rate constant k_{et} of the TiO₂-B nanowire sample is much higher than that of the P25 sample. This result is in agreement as reported that the TiO₂-B nanowire displayed simultaneously excellent n-type electronic conductivity and lithium-ion transport abilities.⁸ In addition, it should be mentioned that during the nanowire EFEPAS measurements, when the applied external potential was below 0.2 V, the maximum photocurrent density was increased by increasing the external applied potential. This phenomenon indicates shallow trapping states existing in the materials, where the trapped electron could be released by applying the weak electrical field, hence the photocurrent increases.

The synthetic TiO₂-B nanowires show relatively high charge carriers transfer ability; additionally with a high surface-to-volume ratio based on the nanoscale structures, one can expect absorption and dissociation of water molecules under the increased humidity and therefore the increase of the conductivity. Zhang et al. reported humidity sensors based on ZnO nanorods and nanowires recently.²⁶ And Schaub et al. determined that oxygen vacancies in the surface layer were responsible for the dissociation of water molecules adsorbed on TiO₂, which was through the transfer of one proton to a nearby oxygen

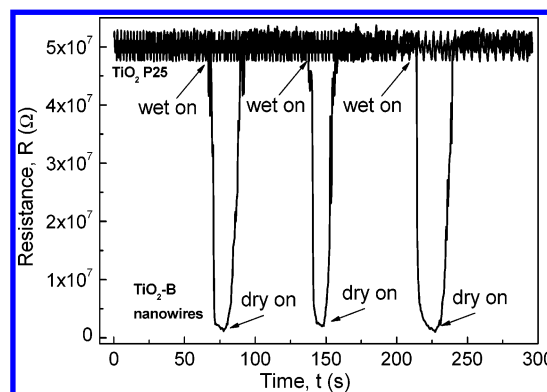


Figure 7. Changes of resistance in the humidity sensors based on TiO₂ P25 nanoparticles and synthetic TiO₂-B nanowires fabricated on surface structured ITO glass substrate with the electrode gap of 50 μ m and the external applied potential of 5 V.

atom, forming two hydroxyl groups for every vacancy. The amount of water dissociation is limited by the density of oxygen vacancies present on the clean surface exclusively.²⁷ Thus, we fabricated humidity sensors using the synthesized TiO₂-B nanowires and TiO₂ P25 nanoparticles for comparison purposes. The results are shown in Figure 7; following the switching of relative humidity, the resistance changes were detected in the synthetic TiO₂-B nanowire-based sensor at room temperature. When RH increased from 5% to 95%, about one and half orders of magnitude change in resistance was observed in the nanowire-based sensor. However, there was no resistance change observed in the P25 nanoparticle-based sensor. The high humidity sensing ability of the TiO₂-B nanowire sensor indicates the level of oxygen vacancies in the nanowire sample is much higher than those in P25 nanoparticles, which promotes the water dissocia-

tion and results in the enhancement of the humidity sensing ability of the nanowire sensor. This is consistent with the results based on MS measurements. Several factors including surface area, densities of oxygen vacancy and dopant, charge-transfer properties, etc. contribute to the humidity sensitivities of the nanomaterials. Hence even TiO₂ P25 owns a three times higher value of surface area than that of TiO₂-B nanowires, but the low densities of oxygen vacancy and dopant, poor charge-transfer ability, and existence of deep trapping states all limit its humidity sensing ability. It should be noted that the sensing properties presented here were obtained for several-micrometer-thick films. For thinner films even higher changes could be observed. The humidity sensitivity could be multiplied by increasing the applied external potentials on the sensors. Therefore, the TiO₂-B nanowires show a potential application as humidity sensors.

4. Conclusions

The single-crystalline TiO₂-B nanowires were successfully synthesized through a facile solvothermal route by control of the solvent and sintering temperature. By analyzing the experimental data with a simple method based on electric field-effected photocurrent action spectra and Mott-Schottky measurements, we revealed that the TiO₂-B phase played an important role in the photoelectrochemical processes. The synthetic TiO₂-B nanowire-based electrode exhibited unique electronic properties, e.g., favorable charge-transfer ability, negative-shifted appeared flat-band potential, existence of abundant surface states or oxygen vacancies, and high level donor density. Moreover, the obtained TiO₂-B nanowires were found to display excellent humidity sensing abilities as functional materials in the application of humidity sensors. Therefore, this study is of importance for developing new functional materials with promising applications in solar energy conversion, photocatalysis, and sensors.

Acknowledgment. This work was financially supported by the National Natural Science Foundation of China (Nos. 20435010 and 20125513), and A Foundation for the Author of National Excellent Doctoral Dissertation of PR China.

References and Notes

- (1) Chambers, S. A.; Thevuthasan, S.; Farrow, R. F. C.; Marks, R. F.; Thiele, J. U.; Folks, L. *Appl. Phys. Lett.* **2001**, 79, 3467.
- (2) Kumazawa, N.; Islam, M. R.; Takeuchi, M. *J. Electrochem. Chem.* **1999**, 472, 137.
- (3) Ohko, Y.; Tatsuma, T.; Fujii, T.; Naoi, K.; Niwa, C.; Kubata, Y.; Fujishima, A. *Nature Mater.* **2003**, 2, 29.
- (4) Gao, X.; Zhu, H.; Pan, G.; Ye, S.; Lan, Y.; Wu, F.; Song, D. *J. Phys. Chem. B* **2004**, 108, 2868.
- (5) Wang, Y. G.; Wang, Z. D.; Xia, Y. Y. *Electrochim. Acta* **2005**, 50, 5641.
- (6) Carp, O.; Huisman, C. L.; Reller, A. *Prog. Solid State Chem.* **2004**, 32, 33.
- (7) Wu, D.; Liu, J.; Zhao, X. N.; Li, A. D.; Chen, Y. F.; Ming, N. B. *Chem. Mater.* **2005**, 18, 547.
- (8) Armstrong, A. R.; Armstrong, G.; Canales, J.; Bruce, P. G. *Angew. Chem., Int. Ed.* **2004**, 43, 2286.
- (9) Feist, T. P.; Davies, P. K. *J. Solid State Chem.* **1992**, 101, 275.
- (10) Armstrong, A. R.; Armstrong, G.; Canales, J.; Garcia, R.; Bruce, P. G. *Adv. Mater.* **2005**, 17, 862.
- (11) Armstrong, G.; Armstrong, A. R.; Canales, J.; Bruce, P. G. *Electrochem. Solid-State Lett.* **2006**, 9, A139.
- (12) Nuspl, G.; Yoshizawa, K.; Yamabe, T. *J. Mater. Chem.* **1997**, 7, 2529.
- (13) Zhu, J.; Zhang, J.; Chen, F.; Anpo, M. *Mater. Lett.* **2005**, 59, 3378.
- (14) Koval, C. A.; Howard, J. N. *Chem. Rev.* **1992**, 92, 411.
- (15) Park, J. H.; Kim, S.; Bard, A. J. *Nano Lett.* **2006**, 6, 24.
- (16) Wang, G. Ph.D. thesis, Charles University, Prague, 2004.
- (17) Zukalova, M.; Kalbac, M.; Kavan, L.; Exnar, I.; Graetzel, M. *Chem. Mater.* **2005**, 17, 1248.
- (18) Li, F. X.; Wang, Y.; Wang, D. Z.; Wei, F. *Carbon* **2004**, 42, 2375.
- (19) Zaban, A.; Meier, A.; Gregg, B. A. *J. Phys. Chem. B* **1997**, 101, 7985.
- (20) Tse, K. Y.; Nichols, B. M.; Yang, W.; Butler, J. E.; Russell, J. N., Jr.; Hamers, R. J. *J. Phys. Chem. B* **2005**, 109, 8523.
- (21) Park, S. M.; Yoo, J. S. *Anal. Chem.* **2003**, 75, 455.
- (22) Fabregat-Santiago, F.; Garcia-Belmonte, G.; Bisquert, J.; Bogdanoff, P.; Zaban, A. *J. Electrochem. Soc.* **2003**, 150, E293.
- (23) Hagfeldt, A.; Bjorksten, U.; Gratzel, M. *J. Phys. Chem.* **1996**, 100, 8045.
- (24) Zhu, Y. *Handbook of Electrochemical Data*; Hunan Sci. Technol., 1985.
- (25) Lewis, N. S. *Inorg. Chem.* **2005**, 44, 6900.
- (26) Zhang, Y.; Yu, K.; Jiang, D.; Zhu, Z.; Geng, H.; Luo, L. *Appl. Surf. Sci.* **2005**, 242, 212.
- (27) Schaub, R.; Thosttrup, P.; Lopez, N.; Lagsgaard, E.; Stensgaard, I.; Norskov, J. K.; Besenbacher, F. *Phys. Rev. Lett.* **2001**, 87, 266104-1.